

The Dynamics of Surface Acoustic Wave-Driven Scaffold Cell Seeding

Melanie Bok, Haiyan Li, Leslie Y. Yeo, James R. Friend

Department of Mechanical and Aerospace Engineering, Micro/Nanophysics Research Laboratory, Monash University, Clayton, Victoria 3800, Australia; telephone: 61-3-9905-3834; fax: 61-3-9905-4943; e-mail: leslie.yeo@eng.monash.edu.au

Received 29 October 2008; revision received 9 December 2008; accepted 10 December 2008

Published online 6 January 2009 in Wiley InterScience (www.interscience.wiley.com). DOI 10.1002/bit.22243

ABSTRACT: Flow visualization using fluorescent microparticles and cell viability investigations are carried out to examine the mechanisms by which cells are seeded into scaffolds driven by surface acoustic waves. The former consists of observing both the external flow prior to the entry of the suspension into the scaffold and the internal flow within the scaffold pores. The latter involves micro-CT (computed tomography) scans of the particle distributions within the seeded scaffolds and visual and quantitative methods to examine the morphology and proliferation ability of the irradiated cells. The results of these investigations elucidate the mechanisms by which particles are seeded, and hence provide valuable information that form the basis for optimizing this recently discovered method for rapid, efficient, and uniform scaffold cell seeding. Yeast cells are observed to maintain their size and morphology as well as their proliferation ability over 14 days after they are irradiated. The mammalian primary osteoblast cells tested also show little difference in their viability when exposed to the surface acoustic wave irradiation compared to a control set. Together, these provide initial feasibility results that demonstrate the surface acoustic wave technology as a viable seeding method without risk of denaturing the cells.

Biotechnol. Bioeng. 2009;103: 387–401.

© 2009 Wiley Periodicals, Inc.

KEYWORDS: surface acoustic wave; cell seeding; tissue engineering; microfluidics; biomaterials; stem cell

Introduction

Tissue engineering is an emerging technology by which a patient's own cells can be seeded into a three-dimensional biodegradable and biocompatible scaffold matrix (Langer and Vacanti, 1993). This extracellular matrix can then be

implanted in vivo to replace an organ/tissue or to recover damaged or defective tissue function without the need for allograft transplantation and the immunosuppressant regimen required to sustain allograft tissue (Chen et al., 2001). It is therefore a promising technology for supplying patients with specialized tissue constructs for wounds that cannot easily be grafted, or as a viable alternative to tissue/organ transplant surgery, which is not only costly but also fraught with risk and exacerbated by the long wait times due to inadequate donor supply (Cheung et al., 2007). In addition, tissue engineering also has the advantage of overcoming biocompatibility and immunological problems commonly encountered during transplant surgery (Martin et al., 2007).

In order for in vitro cell culture to take place within the extracellular matrices, the desired cells first need to be seeded into the scaffold while limiting any denaturing or lysis of the cells (Langer and Vacanti, 1993). Achieving homogeneity in the cultured tissues is also clearly dependent on the uniformity of the cell distribution within the scaffolds and the efficiency of the seeding process (Freed et al., 1994; Soletti et al., 2006). Traditionally, the scaffolds have been seeded using static methods, wherein cell suspensions are allowed to perfuse into the scaffold pores, driven by gravity. However, it is difficult to obtain uniform cell seeding, essential for achieving homogeneity in the final tissue structure (Bueno et al., 2007; Freed et al., 1994) without the application of external forces, since the microarchitecture of the scaffolds is usually complex and the penetration of cells through the scaffold is usually insufficient or superficial. This leads to non-uniform cell distributions wherein the cells only proliferate around the periphery of the scaffold (Burg et al., 2000; McFetridge et al., 2004; Zhao and Ma, 2005). Many studies have reported that new bone tissue is easy to form at the surface of scaffolds but difficult to regenerate at the center of porous scaffolds because more cells collect on the surface of the scaffold than in the inner part of the structure using conventional cell seeding methods (Dong et al., 2002; Yoshikawa et al., 1996).

Correspondence to: L.Y. Yeo

Contract grant sponsor: Australian Research Council Discovery

Contract grant numbers: DP0666660; DP0773221

Seeding homogeneity has direct consequences on improved mechanical stability, faster tissue growth, superior tissue properties (e.g., strength and elasticity) and less damage or loss of function of the tissue once transplanted (Freed et al., 1994). Moreover, with uniform distributions, cells are able to grow in an improved physiological environment that is able to better manage cell wastes and oxygen needs; this is especially important, in particular, for cells sensitive to hypoxia (Radisic et al., 2003).

In addition, the seeding process is slow, taking from hours to days, due to the large capillary resistance arising from the tiny scaffold pores (Woo et al., 2003), typically on the order of 100 μm . These long seeding times can result in adverse effects wherein cells may expire, age beyond their useful state, or lose their viability. The loss of viability, in particular, affects the cells' adhesion, proliferation, and differentiation processes (Wendt et al., 2003). Nevertheless, static seeding methods are still commonly used in tissue culture due to their simplicity (Glicklis et al., 2000; Maquet et al., 2000; Ranucci and Moghe, 1999). Other dynamic methods such as mechanical agitation (Kim et al., 1998) and centrifugation driven by various external forces such as electric/magnetic fields, vacuum (Bowlin and Rittgers, 1997; Ito et al., 2005; Soletti et al., 2006) have also been proposed to seed cells more rapidly and efficiently.

High seeding efficiencies have been achieved through another dynamic seeding method involving oscillatory perfusion (Alvarez-Barreto and Sikavitsas, 2007; Alvarez-Barreto et al., 2007). This technique involves housing the scaffold within a cartridge, which is confined within the perfusion chamber of a bioreactor. The cell suspension is then forced through the construct by applying an oscillatory flow via a peristaltic pump, the flow direction of which is periodically reversed; the 5 min cycle time is set to be sufficiently long to ensure sufficient cell penetration into the scaffold prior to flow reversal. Whilst efficient, such perfusion methods are typically slow, taking 1–2 h, and require large fluid pumps to overcome the capillary resistance imposed by the small scaffold pores, thus restricting the possibility for miniaturization into microfluidic devices.

More recently, the authors have demonstrated the use of surface acoustic waves (SAWs) to drive cell suspensions into the scaffolds (Li et al., 2007a). A SAW is an electroacoustic wave propagating along the surface of a single-crystal piezoelectric substrate with an amplitude of around 10 nm. The ability of SAWs to drive microfluidic actuation lies in the fluid–structural coupling, which arises when fluid is introduced atop the substrate carrying the acoustic wave (Yeo and Friend, 2009). Due to the mismatch in the sound velocities in the substrate and fluid phases, approximately a third of the total energy of the SAW diffracts into the liquid at an angle $\theta = \sin^{-1}(c_l/c_s)$, known as the *Rayleigh angle*, as illustrated in Figure 1a; c_l and c_s are the sound velocities in the liquid and substrate, respectively. If the SAW has sufficient amplitude, a bulk longitudinal pressure wave is generated which drives liquid recirculation within the drop known as *acoustic streaming* (Bradley, 1996).

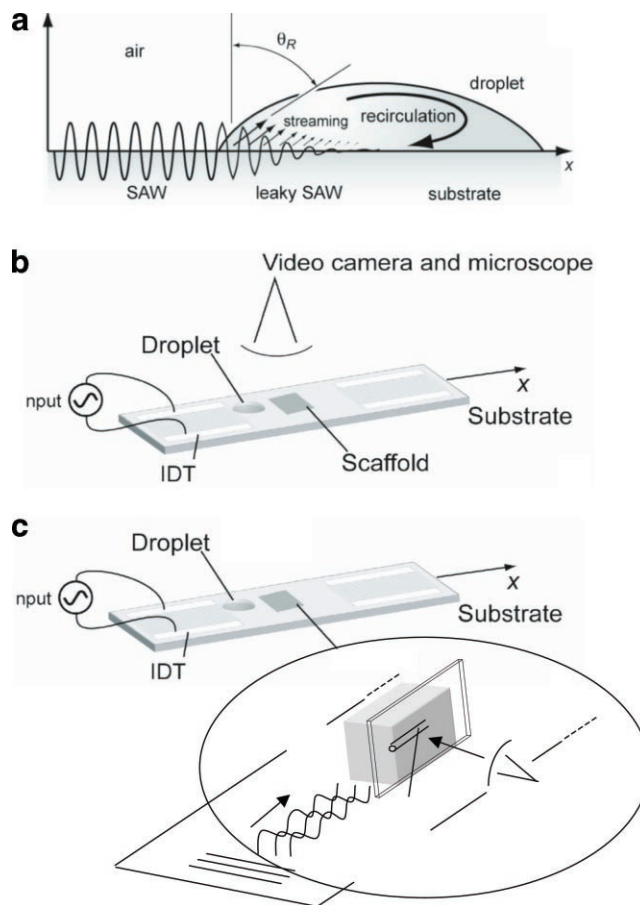


Figure 1. a: Fluid–structural coupling between the SAW and a liquid drop placed on the substrate surface in its path results in the leakage of SAW radiation into the drop at the Rayleigh angle θ_R due to the mismatch in the sound velocities between the substrate and liquid phases. As a result, a longitudinal pressure wave arises which generates bulk liquid recirculation within the drop, also known as acoustic streaming. In addition, a net body force arises on the drop in the direction of the SAW propagation, which at powers beyond a certain threshold level, causes the drop to translate along the substrate in this direction. b: By placing a scaffold behind a drop containing a suspension of cells, it is possible to harness the drop translation to drive the liquid in the drop into the pores of the scaffold. c: Schematic of the experimental setup for visualizing the flow within the scaffold pores. The scaffold was sliced longitudinally exposing its pores to one face. As shown in the inset, a microscope slide was glued onto this face through which the flow through the pores can be observed.

Also, due to the energy diffraction into the drop at the Rayleigh angle, a net body force is produced in the direction of the SAW propagation. Above a critical input power, therefore, it is possible to translate a drop across the substrate surface at velocities up to 1 cm/s. This has previously been employed to move and manipulate drops in open microfluidic platforms or to collect micro/bio-particles deposited onto the substrate surface (Tan et al., 2007a). Other microfluidic manipulations have also been demonstrated using SAW, for example, micromixing (Shilton et al., 2008; Sritharan et al., 2006; Tseng et al.,

2006), micro/bio-particle concentration (Li et al., 2007b, 2008; Shilton et al., 2008), microchannel pumping (Tan et al., 2007b, 2008) and atomization (Alvarez et al., 2008a,b; Friend et al., 2008; Qi et al., 2008). By employing SAW to move a drop consisting of a particle/cell suspension in the direction of the scaffold, as depicted in Figure 1b, it is then possible to drive the fluid and hence the particles/cells into the scaffold. Typical seeding efficiencies of around 85% were achieved and the cells were observed to be seeded into the scaffolds in under 10 s through a simple and straightforward low-cost device, thus suggesting that the SAW is a promising and viable alternative to present static and dynamic seeding methods.

In this article, we attempt to elucidate the fluid flow mechanisms by which the particles or cells are seeded into the scaffold under SAW-driven perfusion. Both external flow in the drop prior to the entry of the liquid into the scaffold and internal flow within the scaffold pores will be examined using high-speed video fluorescence microscopy. Whilst the former is straightforward, visualizing the flow within the micropores is not, and to the best of our knowledge, has not been reported previously. Within this context, there have been some studies in the literature on the bulk hydrodynamics of cell culture scaffold perfusion (Bilgen et al., 2006) and cell seeding in bioreactors (Kim et al., 1998), but none of these relate to the flow within the scaffold pores during cell seeding. In addition, we also carry out micro-CT (computed tomography) scans of the seeded scaffolds to obtain reconstructions in all three dimensions of the cell-scaffold composite matrix, facilitating a more accurate three-dimensional, quantitative description of the seeding efficiencies throughout the scaffold than that obtained previously through a crude slicing method (Li et al., 2007a). Our use of the micro-CT scans for visual inspection of the particle distribution within the scaffold also demonstrates that this non-destructive technique can be used in a practical setting for immediate post-seeding assessment prior to clinical implantation.

In any case, the motivation for these flow studies is to provide a better understanding of the way the fluid enters the scaffold and the manner that particles deposit within the scaffold pores. With these insights, practical strategies to enhance the seeding efficiency and uniformity can then be developed. Finally, we conclude with a brief discussion about the effects of the SAW irradiation on the viability of the cells, in particular, yeast cells and primary murine osteoblast cells. Cell viability is of critical importance since it affects the cells' ability to adhere, proliferate, and differentiate (Wendt et al., 2003). With other dynamic seeding methods, cell denaturing due to membrane lysis induced by subjecting the cells to shear gradients (Bueno et al., 2007) or cell apoptosis due to triggering of intracellular signaling by a cell under duress (Soletti et al., 2006) has been known to occur, thus rendering the seeded cells ineffective. We therefore carry out a brief study to confirm that the SAW irradiation does not adversely affect the cells.

Materials and Methods

Scaffolds

Two different biodegradable and biocompatible scaffolds were used; one hydrophobic to water and the other hydrophilic. The hydrophilic scaffold consisted of commercially available synthetic and porous hydroxyapatite (HA; Apapore, ApaTech, UK) with an average pore size of 246 μm , standard deviation 195 μm , and porosity 25–60% (manufacturer's specifications). The scaffolds were ground to form cubic shapes measuring approximately 5 mm \times 6 mm \times 5 mm using a high speed abrasive disk grinder (DREMEL 15"/16") at 6000 rpm. Loose particles were then removed from the scaffold exterior. The contact angle for a sessile water drop on a solid HA surface, measured experimentally by visual inspection, is $30^\circ \pm 3^\circ$.

Poly- ϵ -capro-lactone (PCL; Sigma Chemical Co., St. Louis, MO) scaffolds, with a molecular weight of 65,000 and a melting point of 65.1°C, on the other hand, were prepared using a conventional solvent casting-particulate leaching method (Li and Chang, 2004; Li et al., 2007a) in which powdered PCL is dissolved within chloroform to a concentration of 10% (w/v). Sodium chloride (NaCl, 100–150 μm) particles were then sieved and incorporated into the suspension at a NaCl/polymer (w/w) concentration ratio of 1.9, which was subsequently cast into a 60 mm Teflon mould. By air-drying the samples under a fume hood for 24 h and vacuum-drying at 60°C for 48 h, the solvent was allowed to evaporate completely. The dried polymer/NaCl composite samples were then submerged in deionized water to leach out the NaCl porogens resulting in 100–150 μm sized pores, before repeating the vacuum drying process again. The resulting scaffolds were then cut carefully with a razor blade into 3 mm \times 5 mm \times 5 mm cubes and stored within a dessicator. The scaffold porosity, as measured using the method of Yang et al. (2002), is approximately $90 \pm 1.5\%$. The contact angle, measured experimentally by visual inspection, for a sessile water drop placed on the synthesized PCL scaffold is around $130 \pm 3^\circ$.

SAW Generation

The SAW is generated by applying an input oscillating electrical signal to an interdigital transducer (IDT) electrode with 25 straight finger pairs in a simple repeating pattern with 100 μm spacing, fabricated using standard photolithography onto a 0.75 mm thick 127.68° Y-X axis rotated cut, X-propagating single-crystal piezoelectric (lithium niobate, LiNbO₃, Roditi, London, UK) substrate. The wavelength λ of the SAW depends on the width and gap of an IDT finger and is around 440 μm in this work, giving rise to a corresponding resonant frequency $f = c_s/\lambda$ of 19.6 MHz, at which we drive the input signal. Essentially, the IDT converts the applied radio frequency (RF) signal into an axial-surface-normal polarized (Rayleigh) wave that

travels with almost no dispersion along the surface of the substrate.

Particle/Cell Seeding and Flow/Particle Distribution Imaging

The SAW-driven particle/cell seeding process is carried out by first diluting a 1% (w/v) solution with original particle concentration 1.4×10^8 particles/mL using deionized water to obtain a final particle concentration of approximately 3.9×10^6 particles/mL. A 10 μ L drop containing this particle/cell suspension is then pipetted onto the surface of the substrate between the IDT where the SAW is generated and the scaffold, as shown in Figure 1b. Due to the net body force arising as a consequence of the diffraction of the SAW radiation into the drop, the drop translates with velocities between 1 mm/s and 1 cm/s towards the scaffold. As it comes into contact with the scaffold, the fluid is then forced into the scaffold pores; the seeding process is considered complete when there is no longer any fluid left on the substrate.

To allow visualization of the flow, we employ 5 μ m green spherical fluorescent polystyrene (PS) microparticles (Duke Scientific, Waltham, MA) as a model system for the cells. This particle size was chosen to mimic the dimensions of undifferentiated bone marrow stromal RS stem cells that are typically 7 μ m in diameter. The particle suspension was observed using a reflection fluorescence stereomicroscope (Olympus BXFM, Tokyo, Japan) at 5X magnification connected to a high speed video imager (Olympus iSpeed, Tokyo, Japan) with a frame capture rate set between 60 and 200 frames/s, and 1 \times shutter speed; the exposure time of the camera was therefore 0.017 or 0.005 s, respectively.

To visualize the flow within the pores with the same high speed microscopic imaging techniques above, we glued the ground smooth long cross-section of the scaffold to a glass microscope slide, with its bottom edge aligned with the lower edge of the slide, ensuring that the contact between the scaffold and slide were as close and as uniform as possible (see Fig. 1c). The microscope slide was mounted vertically on the SAW substrate and at a position about 6 mm from the electrodes where the SAW originates. As illustrated in Figure 1c, we then imaged the process from its side through the transparent microscope slide. The focal plane along which we observed the flow in the pore was sufficiently distant into the pore away from the glass surface to ensure that wall effects are eliminated.

Assessment of the distribution of the seeded particles within the scaffold was carried out using micro-CT (computed tomography; MicroXCT, Xradia, Concord, CA), consisting of a 100 keV, 10 W, 10 μ A tungsten X-ray source. The micro-CT system allows non-invasive and non-destructive three-dimensional scanning of the scaffolds capable of detection, recognition, localization, and characterization down to 1 μ m of the internal features of a material different to the structure of the medium it sits

within. Such scanning can be carried out to a resolution between 1.5 and 30 μ m. The images were acquired using 2 \times binning and 10 s exposure times using 4 \times magnification objectives and 2 \times geometry magnification, swept about a 180 $^\circ$ rotation to obtain 721 projection slices, each therefore representing a 0.25 $^\circ$ axisymmetric slice of the scaffold. Reconstruction of the image slices was carried out using the supplied software (MicroXCT TxM3D Viewer, Xradia) with 2 \times binning, along with beam hardening correction, and shift correction to center the scan; the effective pixel size resolution is 7 μ m. In this case, we employed 90 μ m spherical polystyrene (PS) microparticles (Duke Scientific) in a 1% (w/v) solution containing 1.4×10^8 particles/mL.

Cell Viability Studies

We prepared yeast stock cultures by adding and maintaining 1% yeast extract, 0.5% neutralized bacteriological peptone, and 1% glucose solidified with 1.5% agar (w/v) on standard agar. The media was then autoclaved immediately after preparation at 121 $^\circ$ C and 15 psi for 15 min and the yeast cells grown aerobically to the required cell density at room temperature.

After seeding the scaffolds with the yeast cells under the SAW driving force, we dehydrate these scaffolds with a gradient alcohol solution and mounted them onto stubs. The mounted scaffolds were then coated in gold under vacuum and then observed under scanning electron microscopy (SEM; JEOL-6300F, Tokyo, Japan) using an accelerating voltage of 10 kV. To quantify the ability for the post SAW-treated yeast cells to proliferate in a prolonged culture, we pipetted onto the SAW substrate a yeast suspension with the same volume as that seeded and subjected it to SAW radiation at the input RF power applied to drive the cells into the scaffold. Aliquots of the yeast suspension were then collected and diluted by adding culture media. The initial cell concentration of this suspension was then measured using a haemocytometer (Hausser Scientific, Horsham, PA). The yeast cells were then cultured for an additional 14 days and their concentration in the media were determined at 2, 5, 7, and 14 days.

In order to examine the viability of mammalian cells, primary murine osteoblast cells were isolated using standard techniques. Briefly, long bones or calvaria were isolated from 6 to 8 week-old C57bl/6 mice and flushed from marrow using normal saline. The bones were subsequently minced using bone crushers into smaller particles. They were then subjected to serial collagenase digestions to isolate bone and stromal cell populations. Collagenase activity was halted by the addition of 15% fetal bovine serum (FBS) and the cells were collected at the end of each digestion. The cells were subsequently strained, centrifuged, washed, and resuspended in alpha-MEM (Eagle's minimal essential medium) supplemented with 10–15% FBS and plated (P1) in tissue culture flask for 4 days to allow recovery of cells. At this stage, the cells were removed from the tissue culture flask using trypsin/EDTA, collected, washed, and centrifuged,

resuspended in freeze medium (1×10^6 cells/mL), and frozen under liquid nitrogen vapor until required. Fluorescence-activated cell sorting (FACS; Vantage SE-DiVa, Becton Dickinson, Franklin Lakes, NJ) and a Beckman Coulter analyzer (Cytomics FC500-CXP, Beckman Coulter, Franklin Lakes, NJ) were used to rapidly assess the cell viability following SAW treatment.

Experimental Results

External Flow

Figure 2a shows the translation of the drop prior to and during entry into the scaffold. The higher the applied power,

the faster the translation of the drop. Typically, the drop travels at several mm/s at low input powers and increases quadratically according to the relationship

$$P \sim uF \sim \rho f R^3 u^2 \quad (1)$$

where P is the applied RF power, u the drop translation velocity, F the acoustic force, ρ the fluid density, f the SAW frequency, and R the drop dimension (Li et al., 2007a). The seeding efficiency, defined as the number of particles within the substrate to that in the original suspension, as a function of the drop translation velocity and hence the input power, is shown in Figure 2b, initially increasing sharply from 50% to about 85% with modest increases in the input power

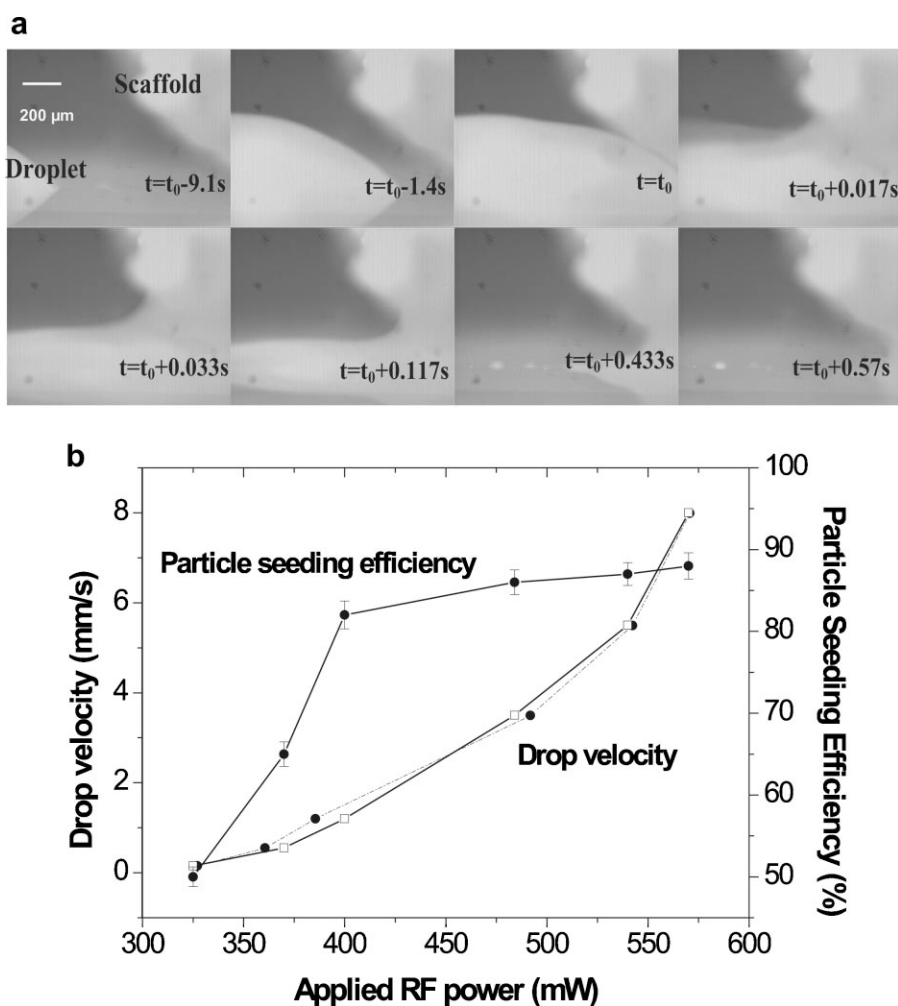


Figure 2. a: Approach and entry of a SAW-driven translating drop containing the particle suspension into the porous HA scaffold. The drop is translating at about 2 mm/s and takes 0.57 s to enter the scaffold completely from the moment initial contact is made with the scaffold. It can be seen from the last frame that the entire drop enters the scaffold, leaving behind only negligible droplet satellite fragments on the substrate. Care was taken to ensure that no fluid circumvented around the periphery of the scaffold by choosing the scaffold dimensions to be substantially larger than the drop. b: The drop translation velocity increases quadratically with the applied RF power, consistent with the scaling in Equation (1), thus providing a greater driving force to push the suspension through the scaffold pores, and hence leading to an increase in the seeding efficiency. Further increasing the power beyond 400 mW, however, does not lead to significant increases in the seeding efficiency, either because of an elastic-plastic transition that the material undergoes that causes it to be lossy and hence to absorb the SAW, or due to the flow limitation through the pore. An upper limit in the seeding efficiency of about 92% is obtained at 570 mW, beyond which no seeding takes place due to atomization of the drop prior to it reaching the scaffold.

325 mW, where the drop velocity is about 0.1 mm/s to 400 mW, where the drop velocity speeds up to about 2 mm/s. Beyond this, further increases in the input power only yielded small increases in the seeding efficiency despite the quadratic increase in the drop velocity from 2 to 8 mm/s. This was previously attributed to the scaffold undergoing an elastic-plastic transition at about 400 mW, which caused the polymeric scaffold material to melt, thereby absorbing the SAW radiation. In light of new evidence from our dynamic visualization experiments, we will provide a plausible alternative explanation for this plateau effect from our current experiments below. In any case, beyond 570 mW, the drop completely atomizes (Friend et al., 2008; Qi et al., 2008) under the large power input before it can reach the scaffold; a maximum seeding efficiency of about 92% can be obtained before this limit is reached.

At 2 mm/s translation speeds, the time when the drop first encounters the scaffold until complete penetration of the

liquid into the scaffold takes place, as shown in Figure 2a, is about 0.57 s for the hydrophilic HA scaffold. For the hydrophobic PCL scaffold, this time is slightly longer, about 1 s. Figure 3a shows the view from above as the drop containing the fluorescent PS particles moves towards the scaffold placed at the top of the images. During drop translation prior to entry into the scaffold, the particles are observed to recirculate azimuthally within the drop due to the effects of acoustic streaming discussed above (Fig. 3a: panel (i)). The azimuthal recirculation, typically 26 mm/s, is a consequence of the asymmetry in the SAW distribution in the drop; this has previously been exploited for other manipulations such as micromixing (Shilton et al., 2008) and particle trapping/concentration (Li et al., 2007; Shilton et al., 2008). However, once the drop comes into contact with the scaffold, the recirculation of the fluid and hence the particles slows down significantly due to the large resistance encountered since the flow passage suddenly narrows into

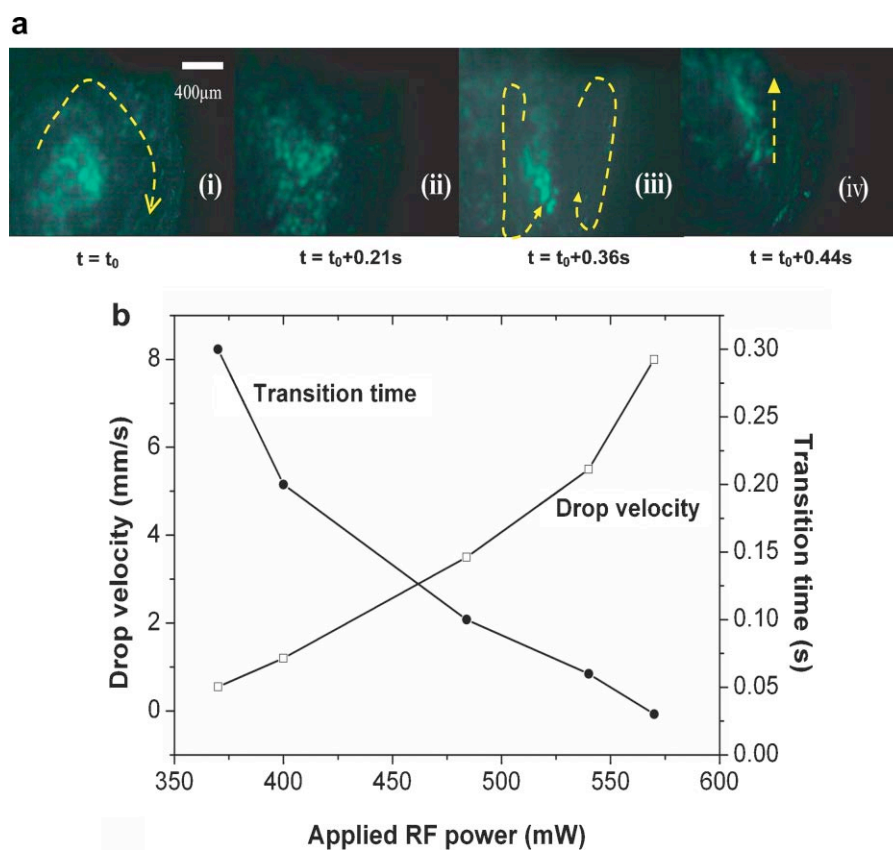


Figure 3. a: Top view of a drop consisting of a suspension of fluorescent particles as it is driven by the SAW into the HA scaffold, obtained through high-speed video microscopy at 200 frames/s. The location of the scaffold is at the top of the images and the drop is therefore being driven from the bottom to the top of the image. Image (i) shows the drop as it is translating, just prior to contact with the scaffold. The arrow indicates the direction of the particle movement and hence shows the azimuthal recirculation of the fluid in the bulk of the drop as it is translating linearly. (ii) The fluid and particle movement suddenly slows down significantly at the instance the drop comes into contact with the scaffold due to the large retardation effect posed by the huge capillary drop across the small scaffold pores. (iii) Transient just after the drop comes into contact with the scaffold in which the bulk of particles and fluid which do not successfully enter the pores are recirculated around into the bulk of the drop. This occurs through a mechanism by which the large resistance imposed by the scaffold gives rise to a pair of recirculating vortices. (iv) After the short initial transient, the fluid and particles which have recirculated are sucked into the pores at high speeds once sufficient back pressure is built up to drive the flow into the pores. b: The relationship between drop velocity, transition time and applied power. Increasing the applied power increases the drop velocity sharply, which only serves to intensify the recirculation transient. [Color figure can be seen in the online version of this article, available at www.interscience.wiley.com.]

numerous parallel pores within the scaffold which are only on average 100 μm in diameter (Fig. 3a: panel (ii)). Due to the sudden retardation of the fast translating drop, an initial transient therefore arises wherein the fluid and particles near the scaffold entry face that do not successfully enter the scaffold pores have to recirculate back into the bulk of the drop before re-attempting their entry into the pores. This sets up a pair of recirculating vortices, as shown in Figure 3a: panel (iii), in a very similar manner to the converging-diverging stagnation flow that arises when fluid directed perpendicularly toward a solid boundary diverges about the axis of the flow; in this case, however, the recirculation sets up the pair of vortices about the flow axis and there is no stagnation point due to the flow passage through the individual pores. In any case, this initial transient lasts only for about 0.1 s, long enough for the pressure in the retarded drop to build up to overcome the capillary pressure imposed by the pores. Once sufficient back pressure is built up, the fluid and particles are sucked quickly into the pores at high speeds of approximately 60 mm/s (Fig. 3a: panel (iv)).

This observation of fluid recirculation, unknown to us in our preliminary work on SAW-driven cell seeding (Li et al., 2007a), may also explain the plateau in the particle seeding efficiency beyond 400 mW seen in Figure 2b. Increasing the applied power and hence the drop translation velocity only serves to intensify the recirculation transient since the pore dimension imposes a restriction on the maximum limiting

velocity through it (Fig. 3b). Moreover, the recirculation does not generate further pressure buildups because of the deformable nature of the drop. We will discuss the effect of the internal flow within the pore and present a simple analytical model by which the pore velocity can be estimated in the next section.

Internal Flow Within the Scaffold Pores

Figure 4 illustrates the dynamics of the flow through a large non-uniform pore several hundred microns in diameter; this specific pore was chosen to facilitate ease of visualization. Although not quantitatively representative of the flow through all the pores of the scaffold due to the wide range of pore sizes and distributions, it at least provides a qualitative picture of how the particles enter and are distributed within the scaffold pores. Due to the non-uniformity of the pore radius, the flow is complex; the flow velocity in the pores varies considerably between 1 mm/s and 1 cm/s. In addition, the majority of particles are convected along the streamlines in the bulk of the fluid away from the boundary layer adjacent to the pore wall; it is well known that particles in the high shear region of the boundary layer migrate towards the low shear regions at the center of microchannels under the influence of shear gradients (Leighton and Acrivos, 1987; Yeo et al., 2006). Sudden expansions in the pore gives rise to fluid recirculation within the expanded cavity regions, as

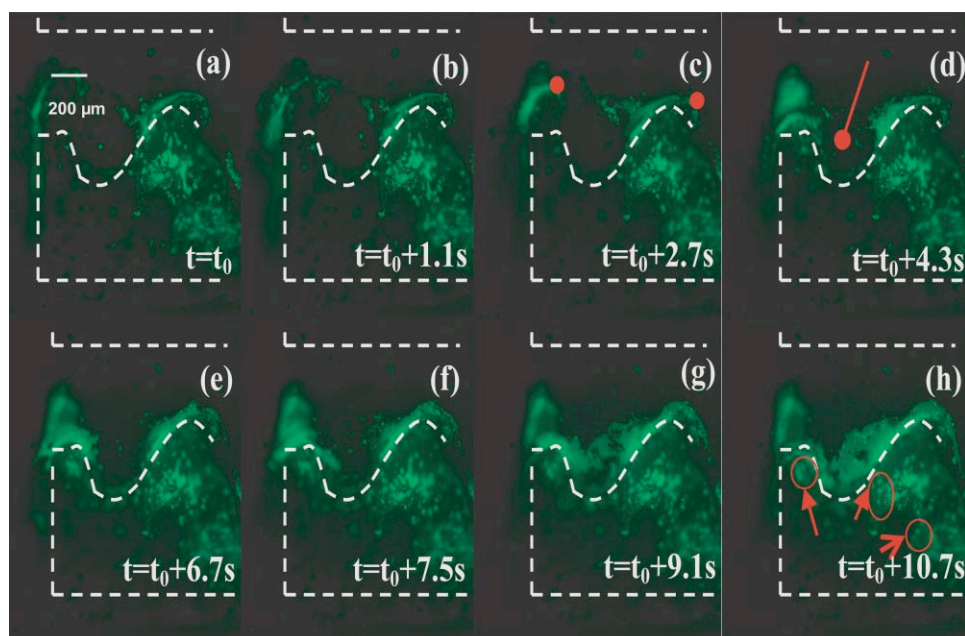


Figure 4. Flow through a large HA scaffold pore, as observed from the side of the scaffold through a cross-sectional slice on which a window is affixed. The dashed lines indicate the rough location of the pore wall although the top wall cannot be seen in the image. Successive images show the advancement of the particle streaklines showing recirculation within the expanded cavity (images (c) and (d)) which enhances the entry of the flow and hence the particles into the smaller secondary pores shown by the circled regions in images (e) through (h). The dots mark the advancing front of the particle streaklines to aid flow visualization. [Color figure can be seen in the online version of this article, available at www.interscience.wiley.com.]

observed in Figure 4: images(d–h). Such recirculation in the expanded pore regions have several counteracting implications on particle seeding within the pores.

On the one hand, the fluid recirculation in the expanded pore sections promote deposition of particles in these regions which would otherwise not have precipitated onto the pore wall since the majority of the particles are convected in the bulk and not within the boundary layer immediately adjacent to the pore wall. Moreover, we observe that the particles do not enter the smaller secondary pores that branch out from the primary pore until this recirculation occurs, as indicated by the late appearance of the particles in these small pores (circled regions) in Figure 4: images (e–h); we note that the instance when recirculation effects start to become significant is observed in Figure 4: images (c–d). This is not surprising since the absence of particles in the boundary layer adjacent to the pore wall stipulates that few particles make the sharp turn into the small secondary pores as most particles flow in the bulk of the large primary pore. It then stands to reason that the fluid recirculation promoted due to the irregularity in the pore size acts to convect particles from the bulk toward the regions adjacent to the pore walls, thus aiding their entry into the secondary pores. In addition, the recirculation alters the primary flow direction such that it is not always in the axial direction of the primary pore and hence perpendicular or obtuse to the direction at which the secondary pores project from the primary pore.

On the other hand, the flow expansion and hence pressure drop due to these large pocket-like cavities in the primary

pore serve to reduce the driving force to effect deeper penetration along the length of the primary pore. Nevertheless, it is altogether possible the recirculation generated by the expansion could reduce this effect since the higher bulk convection velocities and the larger shear stresses acting on the particles in the bulk under the vertical environment allows them to detach from the pore walls and travel further down the pore length, thus aiding deeper penetration into the scaffold. This has been observed widely in other flows through porous media (Civan, 2006). Enhanced diffusion due to Eckart streaming in tortuous substrates has also been reported (Haydock and Yeomans, 2003).

In addition, there is also another phenomenon that arises which could potentially reduce the degree by which penetration into the scaffold is hindered by the pressure drop in the expansion region: Figure 5a shows a sudden acceleration of the liquid meniscus cap front as it moves through the expanded cavity. This can be attributed to a phenomenon known as *capillary bursting* which occurs when a capillary meniscus front encounters a sudden divergence in the pore dimension, as illustrated in the sketch in Figure 5b. We briefly describe the capillary bursting process here as a *speculative* mechanism that could possibly explain pressure buildup and sudden expansion. In the same way that the contact line of a sessile drop placed on an inclined surface is pinned until the platform is tilted sufficiently such that the contact angle of the drop θ exceeds the advancing contact angle of the drop θ_a , that is, $\theta > \theta_a$ (Dussan, 1979), the contact line of the advancing meniscus is pinned at the position where the pore radius begins

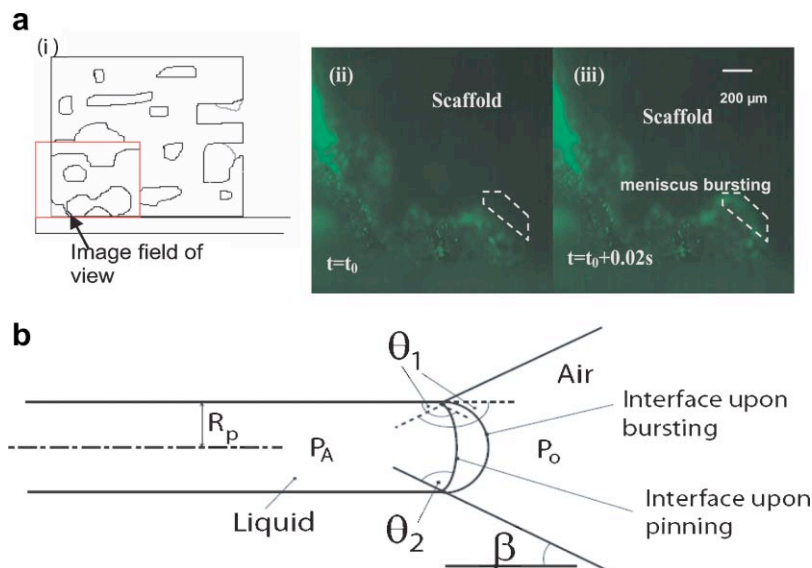


Figure 5. a: Capillary bursting phenomenon in which the capillary meniscus is pinned at the position where the pore radius abruptly diverges, giving rise to the bulging of the meniscus (image (ii)) until the pressure buildup is sufficient to overcome the maximum capillary pressure that the bulging can withstand, as given by Equation (2). Whilst the images shown are for the hydrophilic HA scaffold, similar bursting phenomenon is observed for the hydrophobic PCL scaffolds. The bursting of the capillary once this maximum pressure difference is exceeded leads to an accelerated spontaneous flow within the expanded section (image (iii)) where the curvature decreases progressively. b: Schematic illustration of capillary bursting phenomenon. [Color figure can be seen in the online version of this article, available at www.interscience.wiley.com.]

to abruptly diverge because the new contact angle in the divergent section θ_2 decreases below the contact angle of the meniscus as it was advancing in the previous straight section $\theta_1 = \theta_a$. In fact, the difference between θ_2 and θ_1 is the angle at which the pore diverges β , that is, $\theta_2 = \theta_1 - \beta$. The contact line is therefore pinned at this location and the capillary bulges until the meniscus contact angle θ_b increases from $\theta_1 = \theta_a$ to the new advancing contact angle $\theta_a + \beta = \theta_1 + \alpha$.

The Laplace–Young equation then gives the maximum pressure difference that can be withstood during capillary bulging:

$$\Delta p_b = p_1 - p_2 = -\frac{2\gamma \cos \theta_a}{R_p} \quad (2)$$

where R_p is the pore radius, given that $\theta_b > \theta_a$ for a diverging pore, this pressure difference is always greater than the pressure difference required for the meniscus to advance within a straight pore

$$\Delta p_b = p_1 - p_2 = -\frac{2\gamma \cos \theta_a}{R_p} \quad (3)$$

regardless of the fact that the pore surface is hydrophilic or hydrophobic (Cho et al., 2007). In other words, the meniscus is retarded at the position where the pore radius begins to diverge until the driving pressure exceeds Δp_b , which is the maximum pressure that can be withstood by the bulging meniscus. Once the capillary bursts, however, the meniscus front spontaneously advances into the diverging pore wherein its curvature progressively decreases, as observed in Figure 5. Since the contact angle and hence pressure must return to its equilibrium value as that in the straight pore, the pressure buildup above equilibrium required to unpin the contact line is manifested in the acceleration of the fluid once the contact line is freed.

Although this cannot be seen in the still images given by the figures, the high-speed video images reveal constant oscillatory behavior of the particles as they are convected within the scaffold. It is plausible that such oscillations arise from the vibration of the scaffold sitting atop the SAW substrate, which in turn induces oscillations in the fluid within the pores through a peristaltic action. Such oscillations are believed to further enhance seeding efficiency as well as deposition uniformity within the scaffold. Furthermore, we expect the vibration to aid penetration into the smaller secondary pores. These are consistent with previous studies wherein improved efficiency and distribution have been found when vibration has been employed in various flow environments for cell seeding within scaffolds (Bueno et al., 2007; Li et al., 2001; Wendt et al., 2003).

We now proceed to formulate a simple model for the internal flow through the pore, which is assumed to be long, narrow, straight, and cylindrical such that the lubrication approximation to the Navier–Stokes equation governing

momentum conservation in the fluid applies:

$$\frac{\partial p}{\partial z} = \mu \frac{1}{r} \frac{\partial}{\partial r} \left(r \frac{\partial u}{\partial r} \right) \quad (4)$$

where p is the fluid pressure, μ the viscosity and u the velocity; r and z are the radial and axial coordinates, respectively, assuming axisymmetric cylindrical coordinates. Implicit in the above is the assumption that $R_p \ll L$, where R_p and L is the pore radius and meniscus length, respectively. The latter is defined as the distance into the pore that the liquid has penetrated. Integrating twice subject to the shear free condition $\partial u / \partial r = 0$ at the center of the pore $r = 0$ and the no-slip boundary condition $u = 0$ at the pore wall $r = R_p$, we then obtain a parabolic velocity profile through the pore:

$$u(r) = u_{\max} \left(1 - \frac{r^2}{R_p^2} \right) \quad (5)$$

where $u_{\max} = u(r = 0) = -R_p^2 (\partial p / \partial z) / 4\mu$. Assuming that the flow is fully developed such that the average speed through the pore is equal to the characteristic velocity $U = u_{\max} / 2$, we then have

$$\frac{dL}{dt} = U = -\frac{R_p^2}{8\mu} \frac{\partial p}{\partial z} \sim \frac{R_p^2}{8\mu} \frac{\Delta p}{L} \quad (6)$$

where Δp is the difference between the pressure within the liquid meniscus and external to it, and t denotes the time. The pressure gradient is negative since the fluid pressure at the inlet of the pore is necessarily higher than the atmospheric pressure beyond the meniscus front to drive the fluid flow through the pore.

This pressure differential is given by contributions from the capillary pressure and the pressure arising due to the SAW driving force, that is,

$$\Delta p = \Delta p_{\text{SAW}} - \Delta p_b \quad (7)$$

where Δp_b is given by Equation (3). The SAW pressure can be estimated from the acoustic streaming force density as the SAW radiation leaks into the fluid at the Rayleigh angle θ_R (Frampton et al., 2004):

$$F_x = \rho A^2 \exp(-2\alpha x) \quad (8)$$

where A is the source velocity on the substrate, typically 1 m/s, and α an attenuation coefficient ($\sim 10^{-4}$ Np/m); the direction x is defined along the direction of the SAW as it propagates into the fluid, as specified by the Rayleigh angle. It is then possible to average the force across the cross-section of the front entry face of the scaffold:

$$F_{\text{av}} = \frac{F_x A_d \sin \theta_R}{n A_p} \quad (9)$$

where A_d and A_p is the area of the contact between the drop and the substrate (as defined by the footprint of the drop), and, the pore cross-sectional area, respectively. Given that the decay length scale of the SAW radiation is roughly the drop length scale R_d , the average pressure at the inlet of a single pore due to the acoustic streaming force that provides the driving force for advancing the meniscus through the pores is then

$$\Delta p_{\text{SAW}} = \rho A^2 \phi \sin \theta_R \exp\left(-\frac{2\alpha R_d}{\cos \theta_R}\right) \quad (10)$$

where $\phi = A_p/A_d$ is the scaffold pore fraction.

Substituting Equations (10) and (7) with Equation (3) into Equation (6) then allows us to obtain an estimate of the speed at which the meniscus advances through the pore:

$$\frac{dL}{dt} \sim \frac{R_p^2}{8\mu L} \left[\rho A^2 \phi \sin \theta_R \exp\left(-\frac{2\alpha R_d}{\cos \theta_R}\right) + \frac{2\gamma \cos \theta_R}{R_p} \right] \quad (11)$$

It can be seen that the first term is the SAW pressure that constitutes the driving force for advancing the meniscus through the pores whereas the second term represents the capillary pressure resisting it. For the HA scaffold, we plot the speed of the advancing meniscus front L as a function of its position within the pore from both Equation (11) and from the experimental data in Figure 6. For the theoretical prediction, we use the following parameter values:

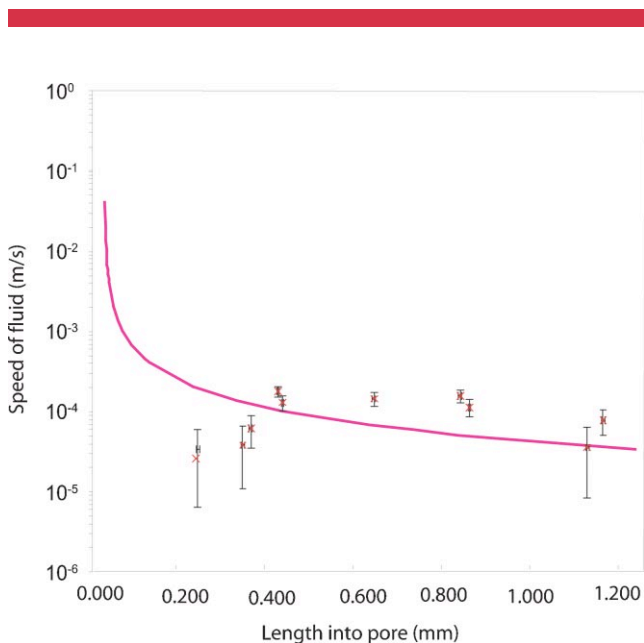


Figure 6. Comparison between the theoretical prediction (solid curve) of Equation (11) and the experimental data (points) for the speed at which the meniscus front advances through the primary pore in Figure 4 of a HA scaffold with its position in the pore. [Color figure can be seen in the online version of this article, available at www.interscience.wiley.com.]

$R_d \sim 1.5$ mm, $R_p \sim 245$ μm , $\phi \sim 0.25$, $\theta \sim 30^\circ$, $\theta_R \sim 22^\circ$, $\mu = 10^{-3}$ kg/ms, and $\rho = 10^3$ kg/m³. It can be seen that the theoretical prediction for the speed of the fluid through the pore agrees reasonably well with the experimental data after a short length into the pore. The theoretical model breaks down in the initial transient over which the flow is developing over an initial entry length region since the model constructed above assumes that the flow is fully developed. Moreover, the lubrication model is not valid at early times when the meniscus length is comparable to the pore dimension, that is, $R_p \sim L$. We have also neglected the tortuosity of the pores and other losses due to viscous and boundary layer effects. The complexity of the flow, such as the recirculation observed, also stipulates that it is not possible to obtain a prediction for the empirical coefficient in the theoretical prediction in Equation (11). This is often the case when considering flow through porous media (Arshad et al., 1993; Civan, 2006). Nevertheless, the relatively good agreement between the slope of the theoretical prediction and the experimental data suggests that the lubrication model is a modest approximation for the internal flow through the pores, at least for a rough estimation of the speed at which the flow occurs.

Seeded Particle Distribution

To investigate the particle distribution within the scaffold, we employ micro-CT scans of the seeded scaffolds. This technique affords both qualitative and quantitative assessment of the effectiveness of the SAW seeding technique within the scaffold without requiring the scaffold to be sliced into thin cross-sections, as was carried out in previous work (Li et al., 2007a), which, not only destroys the scaffold samples but also leads to the possibility of seeded particles being lost during slicing, and therefore not being accounted for in the distribution. Further, the micro-CT scans facilitate a three-dimensional view of the entire scaffold, therefore allowing us to determine the particle distribution relative to the direction in which the scaffold is seeded and hence to assess the importance of the seeding direction, although, after examination of these results, there seems to be little difference that the seeding direction makes. In any case, this factor would appear to be less of a consideration as it is just as easy to drive the suspension drop into any scaffold face using the SAW.

Figure 7 shows the micro-CT scans of the seeded scaffold in the Y - Z cross-sectional plane at various depths along the X -axis, measured from the face where the initial suspension enters the scaffold (indicated by the arrow in the schematic). A quick glance at the particle distributions obtained through dynamic (SAW) seeding (Fig. 7a) and static seeding (Fig. 7b) immediately confirms the effectiveness of using the SAW seeding technique over the static method, both in terms of the particle seeding density as well as the penetration of the seeded particles (>2 mm penetration from the SAW seeding as opposed to approximately 1 mm for the static seeding),

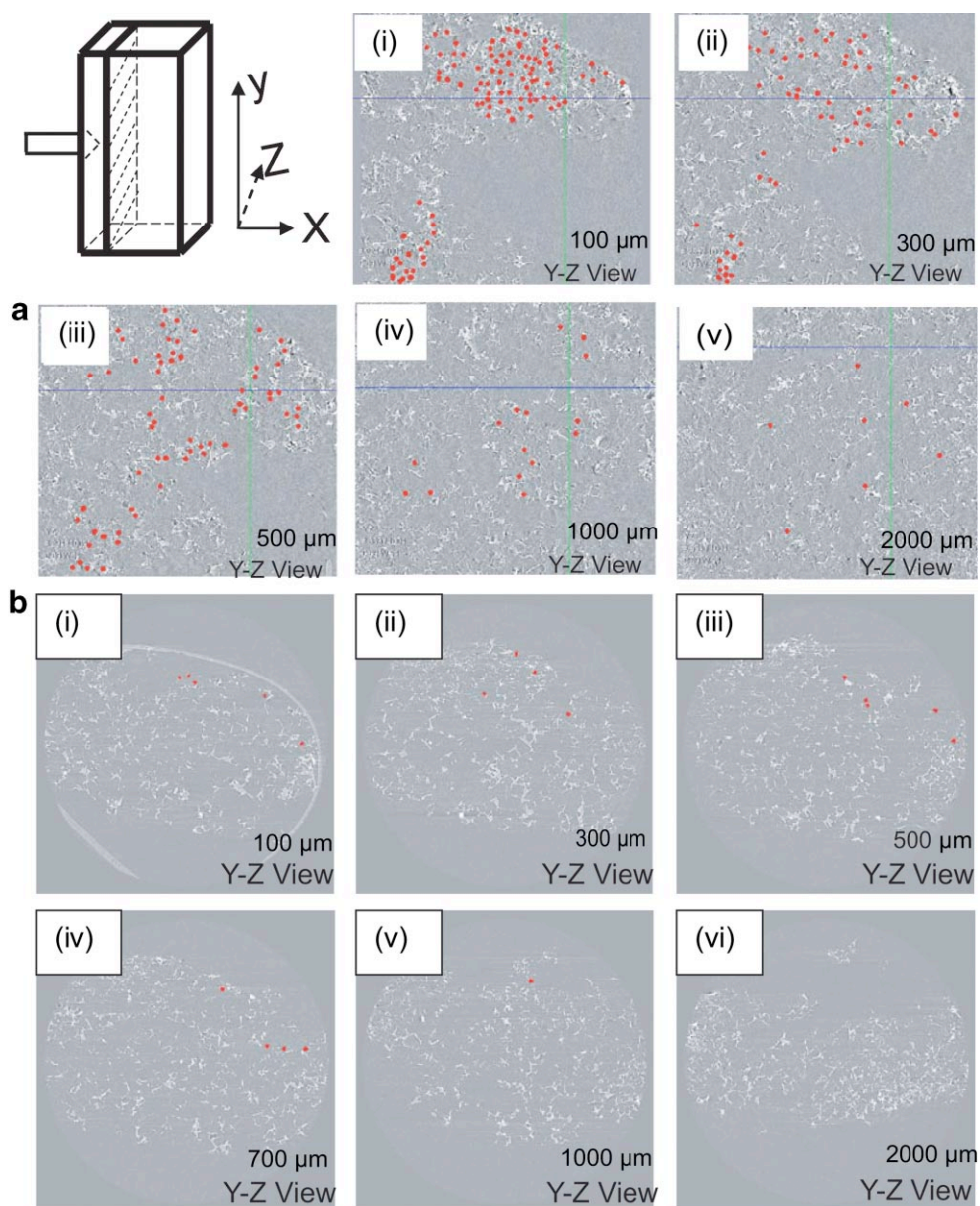


Figure 7. Micro-CT scans across the Y-Z cross-sectional plane as indicated in the schematic. The arrow in the schematic shows the scaffold face through which the drop containing the suspended particles initially enters at $X=0$. The particles are highlighted in red to aid visualization of the otherwise low contrast between them and the scaffold background. The collection of images in (a) are scans at different cross-sectional depths within the scaffold, as measured from $X=0$, for the dynamics (SAW) seeding case whereas the images in (b) are that obtained for the static seeding case. These sets of images clearly show the effectiveness of the SAW seeding technique, not just in terms of the total number of particles seeded but also their penetration (>2 mm for the SAW seeding case as opposed to around 1 mm for the static seeding case) and distribution uniformity. [Color figure can be seen in the online version of this article, available at www.interscience.wiley.com.]

due to the inability of the latter to overcome the large capillary pressure drop within the scaffold pores through gravitational forces alone. A quantitative summary of the scans is shown in Figure 8a, in which we observed that the particles are not only seeded deeper into the scaffold but also more uniformly through the dynamic seeding method. In comparison, the particles are peripherally distributed mainly within the face of the scaffold through which the suspension drop is seeded instead of penetrating deep within the

scaffold. As discussed in the Introduction, this has a profound effect on cell proliferation and hence significantly affects the mechanical structure of the regenerated tissue.

The high speeds at which the suspension drop is forced into the scaffold with the SAW (a drop completely enters into the scaffold in under 5–10 s) means that multiple suspension drops can be delivered into the scaffold with relative ease. We thus examined the micro-CT scans for both the dynamic and static seeding cases to determine the effect

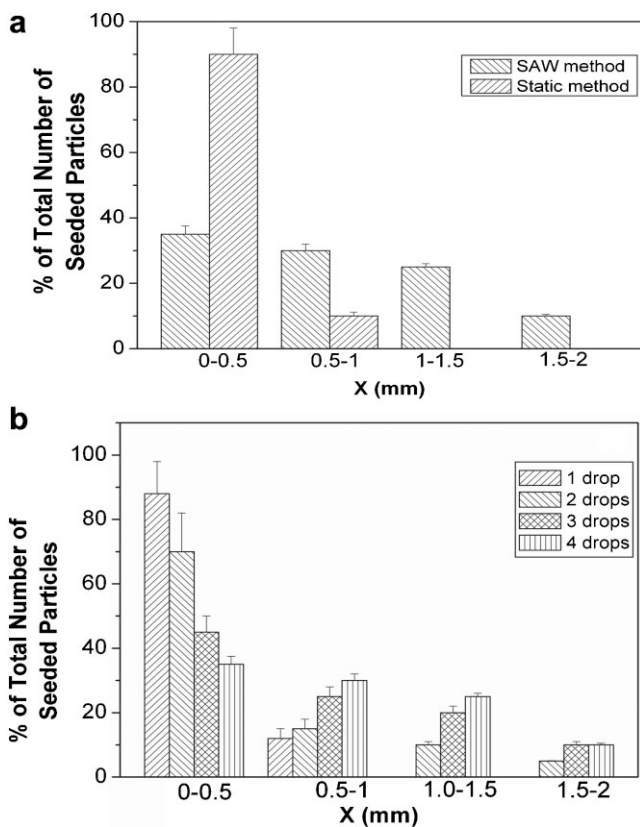


Figure 8. Comparison of the percentage of seeded particles within each 1 mm cross-sectional layer, obtained through image analysis of the micro-CT scans (over the total number of particles seeded) between (a) the dynamic (SAW) and static seeding methods, and how this varies in the SAW seeding method if (b) multiple suspension drops containing the particles are successively driven into the scaffold.

of the insertion of multiple suspension drops on the particle distribution. The results are summarized in Figure 8b. As the number of drops driven into the scaffold increases, we observe that not only does the total number of particles within the scaffold increase but also a more uniform distribution is obtained. With the insertion of four drops, the difference in the particle density between each 0.5 mm thick section is only around 5–10%, which is considerably less than if a single drop were to be driven into the scaffold and significantly less than that if static seeding were employed, which could be as high as 50%.

Cell Viability Studies

The effect of ultrasonic waves on cell viability has been previously investigated, in which it was shown that there was no significant effect on the viability of yeast cells even after application of standing wave ultrasound radiation for up to 2 h (Radel et al., 2000), or the viability of red blood cells in a tubular acoustic resonator (Cousins et al., 2000). To our knowledge, little work, however, has been carried out to

investigate the effects of SAW radiation on biological cells, and in particular, within the context of cell seeding.

Our preliminary results on the viability of yeast cells during the seeding process are nevertheless encouraging. Figure 9a shows SEM images of the PCL scaffold into which yeast cells have been seeded. It can be seen that the cells, which have attached themselves onto the pore walls appear to maintain their original spheroidal/ellipsoidal shape and size. There is therefore little evidence that the cells are fragmented or denatured during the process, as they would appear as smaller non-homogenous particles rather than homogeneous spheres or ellipsoids similar to their original size if this were the case. Figure 9b, on the other hand, shows that post SAW-treated yeast cells continue to proliferate in the prolonged cultured in the subsequent 14 days. In

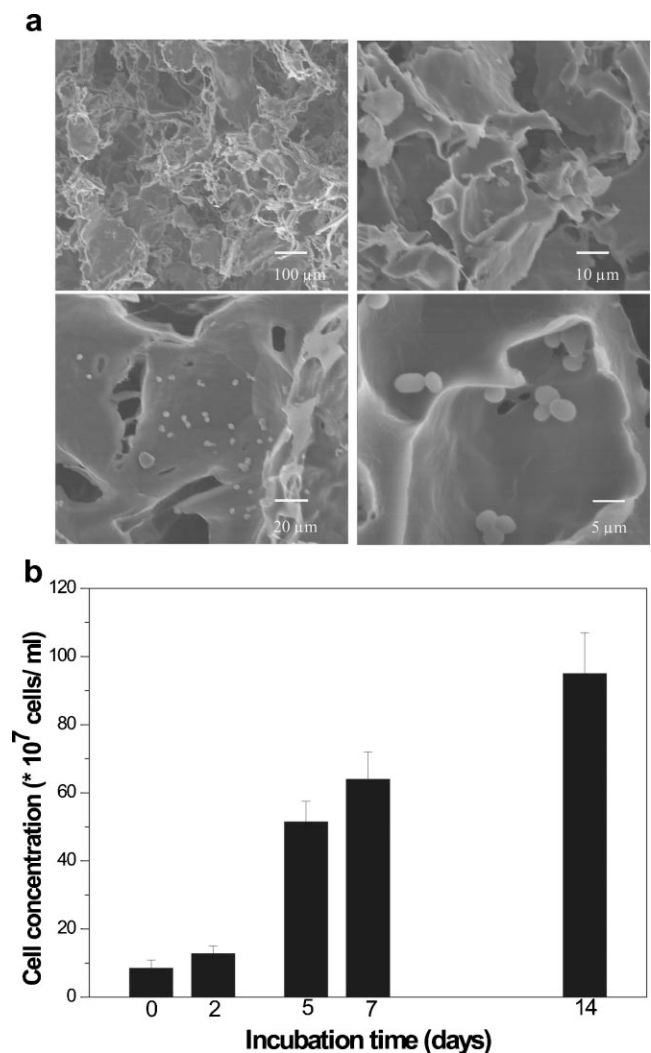


Figure 9. a: SEM images of yeast cells seeded into the scaffolds by SAW actuation. The morphology of the cells does not appear to be compromised by the SAW treatment. b: Proliferation rates of the yeast cells after irradiation with the SAW. The cells are observed to continue proliferating during the subsequent 14-day period, which further confirms their post-treatment viability.

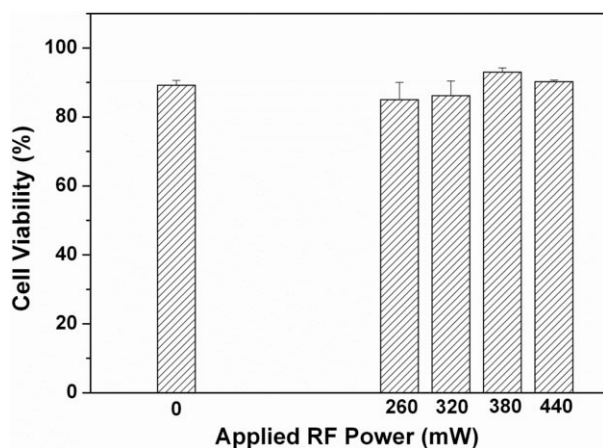


Figure 10. Viability of primary murine osteoblast cells treated by the SAW for 10 s at different RF powers with the control data (no applied power) shown on the left. The cell density is 5000 cells/ μ L and the volume of the cell suspension is 10 μ L. Cells were subject to 20 MHz SAWs for 10 s.

addition, Figure 10 provides evidence that the viability of primary murine osteoblast cells treated by the SAW over a range of applied RF powers from 0 to over 380 mW is not statistically different from that of the cells that are not subject to SAW treatment. We note, however, that at large applied RF powers beyond 440 mW, atomization of the drop containing the cell suspension begins to occur and hence some stem cells were lost to the atmosphere in the process, thus nullifying the results at higher powers.

More in-depth studies are currently being conducted; nevertheless, the uniform size and shapes of the yeast cells and their ability to proliferate after being seeded into the scaffolds under SAW irradiation show that the morphology of the yeast cells seeded within the scaffolds is preserved and that their viability has not been compromised. This is supported by preliminary data using stem cells, which, again, show little effect of the SAW irradiation on the cell viability.

Conclusions

The dynamics of SAW-driven cell seeding in scaffolds has been investigated, from which it is hoped will provide a basis for further optimization of the speed, efficiency and uniformity by which cells are seeded by this method. Our observations of the flow in the drop prior to its entry into the scaffold provide a plausible explanation as to why there exists a curious limitation to increases in the particle seeding efficiency despite the quadratically increasing drop translation velocity as the power is increased. Whilst we have speculated previously using scaling arguments that this can be attributed to a plastic transition in the scaffold elasticity, observations of the particle motion within the drop using high speed microscopy reveal that the sudden flow

restriction imposed by the small scaffold pores requires a large proportion of the fluid and hence the particles to recirculate externally prior to entry. Since the deformable drop shape does not allow significant pressure buildups within the drop, there therefore exists a maximum limiting velocity into the scaffold as determined by the pore size.

Close inspection of the particles as the fluid travels through the pores also provides insight on how the particles are deposited into the large primary and smaller secondary pores. We observe that the flow recirculation that arises in expanded pore sections generally aids the deposition of the particles into the secondary pores by eliminating the boundary layers adjacent to the walls where particles are deficient due to the high shear associated in these layers; in addition, the recirculation generates flow in other directions than that along the axis of the primary pore, which is often perpendicular or obtuse to the secondary pores. The vortices arising from the recirculation in the pore cavities also generates high shear stresses causing particles to detach from the pore walls; together with the higher bulk convection velocities compared to the case for uniform and straight pores, the particles are therefore forced deeper into the scaffold. Capillary bursting and the vibration of the scaffold pores under the SAW excitation thereby generating peristaltic action are other phenomena resulting from abruptly diverging pores that promote deeper particle penetration and entry into secondary pores. Although it is intuitive to think that the non-uniformity in the pore sizes and the existence of expanded pore cavities induces the pressure drop and hence reduces the penetration depth of particles into the scaffold, the existence of these complex phenomena that accompany expansions in the pore size generally provide mechanisms that promote deeper seeding into the scaffold and into the small secondary pores of the scaffold.

We also demonstrate that micro-CT scanning is a practical method for post-seeding assessment of the seeding effectiveness without destroying the scaffold, which thus enables it to be used in clinical settings to ensure sufficient (in terms of total number as well as penetration depth) cells are seeded uniformly into the scaffold prior to in vivo implantation. Both qualitative and quantitative analysis of the micro-CT scans confirm the significant improvement of the particles into the scaffold with SAW seeding as compared with static seeding. Moreover, given that the drop containing the particle suspension enters the scaffold in under 5–10 s with the SAW seeding technique, it is possible to drive multiple drops into the scaffold. Inspection of the micro-CT scans reveal that using multiple drops not only increases the total number of seeded particles but also significantly improves the uniformity of their distribution within the scaffold.

Finally, we demonstrate through preliminary studies that the SAW irradiation does not lead to denaturing of the cells or adverse effects on the ability of the cells to proliferate. SEM images of yeast cells seeded into the scaffolds after exposure to SAWs show little size and morphology

differences to the original untreated cells, suggesting that the cells have not been fragmented or denatured due to the radiation. Moreover, the yeast cells are observed to continue proliferating in prolonged culture over a 14-day study, indicating that their viability has been preserved. Preliminary investigations using primary murine osteoblast cells also show little effect of the SAW radiation on their viability. These results therefore inspire confidence that the SAW is a viable and potentially flexible and powerful method for the rapid, efficient, and uniform seeding of cells into scaffolds.

Support for this project was funded through Australian Research Council Discovery Grants DP0666660 and DP0773221. The authors are also grateful to A. Dasvarma and K. Traianedes (Australian Stem Cell Centre) for help with the preliminary stem cell viability experiments, and P. Pigram and A. Peele (LaTrobe University) for the use of their micro-CT scanning equipment.

References

- Alvarez M, Friend JR, Yeo LY. 2008a. Surface vibration induced spatial ordering of periodic polymer patterns on a substrate. *Langmuir* 24:10629–10632.
- Alvarez M, Friend JR, Yeo LY. 2008b. Rapid generation of protein aerosols and nanoparticles via SAW atomisation. *Nanotechnology* 19:455103.
- Alvarez-Barreto JF, Sikavitsas VI. 2007. Improved mesenchymal stem cell seeding on RGD-modified poly(L-lactic acid) scaffolds using flow perfusion. *Macromol Biosci* 7:579–588.
- Alvarez-Barreto JF, Linehan SM, Shambaugh RL, Sikavitsas VI. 2007. Flow perfusion improves seeding of tissue engineering scaffolds with different architectures. *Ann Biomed Eng* 35:429–442.
- Arshad A, Rahman NS, Rahman SS. 1993. Studies of pressure build-up due to particle deposition in micro-capillary with the use of three-dimensional trajectory analysis. *J Chem Tech Biotech* 58:377–385.
- Bilgen B, Sucusky P, Neitzel GP, Barabino GA. 2006. Flow characterization of a wavy-walled bioreactor for cartilage tissue engineering. *Biotechnol Bioeng* 95:1009–1022.
- Bowlin GL, Rittgers SE. 1997. Electrostatic endothelial cell transplantation within small-diameter (<6 mm) vascular prosthesis: A prototype apparatus and procedure. *Cell Transplant* 6:631–637.
- Bradley CE. 1996. Acoustic streaming field structure: The influence of the radiator. *J Acoust Soc Am* 100:1399–1408.
- Bueno EM, Laevsky G, Barabino GA. 2007. Enhancing cell seeding of scaffolds in tissue engineering through manipulation of hydrodynamic parameters. *J Biotechnol* 129:516–531.
- Burg KJL, Holder WD, Jr., Culberson CR, Beiler RJ, Greene KG, Loeb sack AB, Roland WD, Eiselt P, Mooney DJ, Halberstadt CR. 2000. Comparative study of seeding methods for three-dimensional polymeric scaffolds. *J Biomed Mater Res* 51:642–649.
- Chen G, Ushida T, Tateishi T. 2001. Development of biodegradable porous scaffolds for tissue engineering. *Mater Sci Eng C* 17:63–69.
- Cheung H-Y, Lau K-T, Lu T-P, Hui D. 2007. A critical review of polymer-based bio-engineered materials for scaffold development. *Composites B* 38:291–300.
- Cho H, Kim H-Y, Kang JY, Kim TS. 2007. How the capillary burst micro-valve works. *J Colloid Interface Sci* 306:379–385.
- Civan F. 2006. Temperature effect on power for particle detachment from pore wall described by an Arrhenius-type equation. *Transport in Porous Media* 67:329–334.
- Cousins SM, Holownia P, Hawkes JJ, Limaye MS, Price CP, Keay PJ, Coakley WT. 2000. Plasma preparation from whole blood using ultrasound. *Ultrasound Med Biol* 26:881–888.
- Dong J, Uemura T, Shirasaki Y, Tateishi T. 2002. Promotion of bone formation using highly pure porous beta-TCP combined with bone marrow-derived osteoprogenitor cells. *Biomaterials* 23:4493–4502.
- Dussan VEB. 1979. On the spreading of liquids on solid surfaces: Static and dynamic contact lines. *Annu Rev Fluid Mech* 11:371–400.
- Frampton KD, Martin SE, Minor K. 2004. Acoustic streaming in microscale cylindrical channels. *Appl Acoust* 65:1121–1129.
- Freed LE, Marquis JC, Vunjak-Novakovic G, Emmanuel J, Langer R. 1994. Composition of cell-polymer cartilage implants. *Biotechnol Bioeng* 43:605–614.
- Friend JR, Yeo LY, Arifin DR, Mechler A. 2008. Evaporative self-assembly assisted synthesis of polymeric nanoparticles by surface acoustic wave atomization. *Nanotechnology* 19:145301.
- Glicklis R, Shapiro L, Agbaria R, Merchuk JC, Cohen S. 2000. Hepatocyte behavior within three-dimensional porous alginate scaffolds. *Biotechnol Bioeng* 67:344–353.
- Haydock D, Yeomans JM. 2003. Acoustic enhancement of diffusion in a porous material. *Ultrasonics* 41:531–538.
- Ito A, Ino K, Hayashida M, Kobayashi T, Matsunuma H, Kagami H, Ueda M, Honda H. 2005. Novel methodology for fabrication of tissue-engineered tubular constructs using magnetite nanoparticles and magnetic force. *Tissue Eng* 11:1553–1561.
- Kim B-S, Putnam AJ, Kulik TJ, Mooney DJ. 1998. Optimizing seeding and culture methods to engineer smooth muscle tissue on biodegradable polymer matrices. *Biotechnol Bioeng* 57:46–54.
- Langer R, Vacanti JP. 1993. Tissue engineering. *Science* 260:920–926.
- Leighton D, Acrivos A. 1987. The shear-induced migration of particles in concentrated suspensions. *J Fluid Mech* 181:415–439.
- Li H, Chang J. 2004. Fabrication and characterization of bioactive wollastonite/PHBV composite scaffolds. *Biomaterials* 25:5473–5480.
- Li Y, Ma T, Kniss DA, Lasky LC, Yang S-T. 2001. Effects of filtration seeding on cell density, spatial distribution, and proliferation in non-woven fibrous matrices. *Biotechnol Prog* 17:935–944.
- Li H, Friend JR, Yeo LY. 2007a. A scaffold cell seeding method driven by surface acoustic waves. *Biomaterials* 28:4098–4104.
- Li H, Friend JR, Yeo LY. 2007b. Surface acoustic wave concentration of particle and bioparticle suspensions. *Biomed Microdev* 9:647–656.
- Li H, Friend JR, Yeo LY. 2008. Colloidal island formation and erasure in a microfluidic system induced by surface acoustic wave radiation. *Phys Rev Lett* 101:084502.
- Maquet V, Martin D, Malgrange B, Franzen R, Schoenen J, Moonen G, Jerome R. 2000. Peripheral nerve regeneration using bioresorbable macroporous polylactide scaffolds. *J Biomed Mater Res* 52:639–651.
- Martin I, Miot S, Barbero A, Jakob M, Wendt D. 2007. Osteochondrial tissue engineering. *J Biomechanics* 40:750–765.
- McPetridge PS, Daniel JW, Bodamyali T, Horrocks M, Chaudhuri JB. 2004. Preparation of porcine carotid arteries for vascular tissue engineering applications. *J Biomed Mater Res* 70A:224–234.
- Qi A, Yeo LY, Friend JR. 2008. Interfacial destabilization and atomization driven by surface acoustic waves. *Phys Fluids* 20:074103.
- Radel S, McLoughlin AJ, Gherardini L, Doblhoff-Dier O, Benes E. 2000. Viability of yeast cells in well controlled propagating and standing ultrasonic plane waves. *Ultrasonics* 38:633–637.
- Radisic M, Euloth M, Yang L, Langer R, Freed LE, Vunjak-Novakovic G. 2003. High-density seeding of myocyte cells for cardiac tissue engineering. *Biotechnol Bioeng* 82:403–414.
- Ranucci CS, Moghe PV. 1999. Polymer substrate topography actively regulates the multicellular organization and liver-specific functions of cultured hepatocytes. *Tissue Eng* 5:407–419.
- Shilton R, Tan MK, Yeo LY, Friend JR. 2008. Particle concentration and mixing in microdrops driven by focused surface acoustic waves. *J Appl Phys* 104:014901.
- Soletti L, Nieponice A, Guan J, Stankus JJ, Wagner WR, Vorp DA. 2006. A seeding device for tissue engineered tubular structures. *Biomaterials* 27:4863–4870.
- Sritharan K, Strobl CJ, Schneider MF, Wixforth A. 2006. Acoustic mixing at low Reynold's numbers. *Appl Phys Lett* 88:054102.
- Tan MK, Friend JR, Yeo LY. 2007a. Microparticle collection and concentration via a miniature surface acoustic wave device. *Lab Chip* 7:618–625.

- Tan MK, Friend JR, Yeo LY. 2007b. Surface acoustic wave driven micro-channel flow. Proceedings of the 16th Australasian Fluid Mechanics Conference, Gold Coast, Australia, p. 790–793.
- Tan MK, Yeo LY, Friend JR. 2008. Rapid microchannel fluid actuation and particle manipulation induced by surface acoustic waves. *Phys Rev Lett*, submitted for publication.
- Tseng W-K, Lin J-L, Sung W-C, Chen S-H, Lee G-B. 2006. Active micro-mixers using surface acoustic waves on Y-cut 128° LiNbO₃. *J Micro-mech Microeng* 16:539–548.
- Wendt D, Marsano A, Jakob M, Heberer M, Martin I. 2003. Oscillating perfusion of cell suspensions through three-dimensional scaffolds enhances cell seeding efficiency and uniformity. *Biotechnol Bioeng* 84:205–214.
- Woo KM, Chen VJ, Ma PX. 2003. Nano-fibrous scaffolding architecture selectively enhances protein adsorption contributing to cell attachment. *J Biomed Mater Res* 67A:531–537.
- Yang J, Shi GX, Bei J, Wang SG, Cao YL, Shang QX, Yang G, Wang W. 2002. Fabrication and surface modification of macroporous poly(L-lactic acid) and poly(L-lactic-co-glycolic acid) (70/30) cell scaffolds for human skin fibroblast cell culture. *J Biomed Mater Res* 62:438–446.
- Yeo LY, Friend JR. 2009. Ultrafast microfluidics using surface acoustic waves. *Biomicrofluidics* 3:012002.
- Yeo LY, Hou D, Maheshwari S, Chang H-C. 2006. Electrohydrodynamic surface microvortices for mixing and particle trapping. *Appl Phys Lett* 88:233512.
- Yoshikawa T, Ohgushi H, Tamai S. 1996. Immediate bone forming capability of prefabricated osteogenic hydroxyapatite. *J Biomed Mater Res* 32:481–492.
- Zhao F, Ma T. 2005. Perfusion bioreactor system for human mesenchymal stem cell tissue engineering: Dynamic cell seeding and construct development. *Biotechnol Bioeng* 91:482–493.